

Automated structure discovery for Tip Enhanced Raman Spectroscopy

Harshit Sethi,¹ Markus Junntila,¹ Orlando J. Silveira,^{1,*} and Adam S. Foster^{1,2,†}

¹*Department of Applied Physics, Aalto University, Helsinki, FI-02150, Finland*

²*WPI Nano Life Science Institute (WPI-NanoLSI),*

Kanazawa University, Kakuma-machi, Kanazawa, 920-1192, Japan

Abstract

Tip-Enhanced Raman Spectroscopy (TERS) provides nanoscale chemical fingerprints alongside high-resolution topographic mapping of molecules, offering a powerful tool for materials discovery. However, TERS image datasets are challenging to interpret and typically demand time-consuming, computationally intensive quantum-chemistry calculations. To overcome this problem, we present an encoder–decoder model trained and evaluated on simulated TERS images of planar molecules, enabling direct prediction of molecular structures from spectral simulated data with high accuracy. Our approach demonstrates the feasibility of automating molecular structure identification from TERS images, bypassing traditional manual analysis. These findings provide a foundation for extending machine learning methods to experimental TERS datasets, potentially accelerating molecular discovery by integrating nanoscale spectroscopy with automated computational analysis.

*Electronic address: orlando.silveirajunior@aalto.fi

†Electronic address: adam.foster@aalto.fi

I. INTRODUCTION

Achieving atomic resolution in optical imaging is a central goal for advancing nanoscale science and enabling the study and design of materials. In Scanning Tunneling Microscopy (STM), the functionalization of a tip apex with a single CO molecule enables unprecedented resolution of the internal structure of adsorbed molecules and their orbital densities [1–4]. Similar functionalization in non-contact Atomic Force Microscopy (AFM) provides stunning sub-atomic resolution of the skeletal structure of a molecule [2, 4–6]. Both STM and AFM are among a family of techniques called scanning probe microscopy (SPM), and while it has been proposed that combining different modes of SPM allows for resolution not only the geometric arrangement of the atoms, but also their chemical composition, formidable challenges are still faced to achieve this routinely [7]. In contrast, conventional chemically specific non-destructive spectroscopies, such as infrared and Raman, readily offer chemical characterization, but are constrained by the Abbe diffraction limit and thus lack the type of spatial resolution that CO-tip functionalized SPM can give [8, 9]. However, recent advances have shown that integrating an STM tip to the Raman spectrometer greatly enhances the Raman signal, giving the possibility to render both topographical and chemical information by imaging molecules at the Ångström scale [9–15]. In this integrated technique, named tip enhanced Raman spectroscopy (TERS), an incoming light triggers a collective response to the electrons at the STM tip apex, producing localized surface plasmon excitations and confining propagating light [16] (see Fig. 1). The STM tip acts then as a nanoantenna, transferring to the far-field information from the evanescent waves that originate from interactions of the light with sample sizes smaller than its wavelength, thus overcoming the diffraction limit and limiting the spatial resolution only to the apex radius. Despite these advances, the interpretation of TERS images remains challenging, owing to complex contrast mechanisms, tip dependence, and the large volume and dimensionality of the resulting datasets. Theoretical developments have successfully allowed individual comparisons of simulated TERS images and experiments through visual inspections [12, 17–24], but they can be quite demanding tasks as TERS grows to belong to the mainstream group of experiments for molecular characterization [25, 26]. All these challenges naturally motivate the use of data-driven approaches to assist in extracting physically and chemically meaningful information from such measurements.

Machine learning (ML) methods have been increasingly used in microscopy to assist with the analysis and interpretation of large, noisy, and high-dimensional datasets. Applications include image denoising and reconstruction, feature identification, and the extraction of underlying physical trends that are difficult to access with conventional analysis. In scanning transmission electron microscopy (STEM), for example, CNNs have been applied to STEM images to extract structural and compositional information at high throughput [27]. Domain-adaptation methods such as CycleGANs have been employed to render simulated STEM data more realistic for training, enabling robust identification of single-atom defects [28]. More recently, vision-language transformers have been used to predict atomic structure as captions from STEM images [29]. For SPM in particular, recent advances at the intersection with ML have advanced prospects for autonomous materials discovery [30, 31]. Early supervised ML studies established that SPM images can be mapped directly to atomic-scale structures. For example, by using convolutional neural networks (CNNs) to directly predict likely 2D maps of structures from AFM images [32, 33], or combined with graph neural networks (GNNs) [34] for both STM and AFM [35, 36]. Complementary approaches used multimodal recurrent networks to infer IUPAC names from AFM data [37], and conditional generative adversarial networks (cGANs) to translate AFM images into ball-and-stick representations [38].

In this work, we present **SMARTERS** (Structural Machine Learning for High-Resolution Tip-Enhanced Raman Spectroscopy), an automated CNN-based ML model motivated by the growing use of ML in microscopy and the need for theoretical tools to decode TERS images. Inspired by the success of SPM models trained on simulations, here, the dataset of TERS images was simulated by considering the plasmonic resonance created at the SPM tip as the main source of enhancement of the Raman signal. Within this approach, the local plasmonic field is then treated as a three-dimensional Gaussian function with a specific full width at half maximum (FWHM) [18, 21–23, 39, 40]. Despite the local field created on the tip, it is well known that the interactions of the molecules with the underlying substrate also play an important role in the enhancement of the Raman signal [20, 24], and subtle variations of adsorption geometries may drastically affect the vibrations of the molecules [15]. In our simulations, we considered only isolated molecules, making the model more suitable for planar molecules lying flat on top of weakly interacting substrates, e.g NaCl, where disturbances in the vibrational modes are expected to be less [11]. Additionally, since

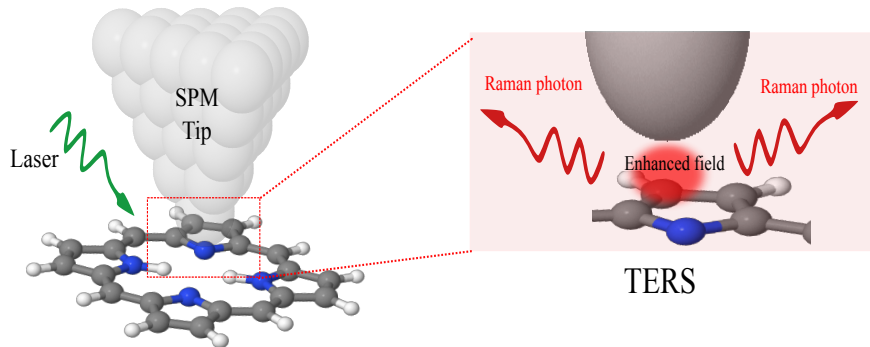


FIG. 1: Schematic illustration of the tip-enhanced Raman spectroscopy (TERS) setup, where laser illumination induces localized field enhancement at the SPM tip apex, enabling enhanced Raman signal intensity.

different molecules exhibit varying numbers of vibrational modes, we proposed a binning procedure along the frequency axes to uniformize the hyperspectral image with different numbers of spectral channels, making the data more suitable for the neural network training.

SMARTERS provides a strong methodological foundation for automated scanning probe microscopy platforms and represents a step toward realizing similar autonomous capabilities in TERS, possibly enabling in the future chemically specific discovery and characterization at the atomic and molecular scale. Automated molecular structure discovery from TERS hyperspectral images has not, to our knowledge, been demonstrated prior to this work. Here, we address that gap by developing and validating ML methods for structural discovery from TERS hyperspectral datasets. Our model serves as a proof of concept for automating molecular structure identification from TERS images and contributes to a better understanding of light-matter interactions.

II. METHODS

We formulate the task of determining the geometry of molecules from TERS data as an image-to-image translation problem. To address this, the methodology used in SMARTERS is centered on training a deep encoder-decoder network on a large-scale, computationally simulated dataset. This process involves curating a cohort of suitable planar molecules, then for each one, generating a synthetic TERS spectral image paired with its ground-truth 2D atomic position map. The TERS images are generated using our Python re-implementation

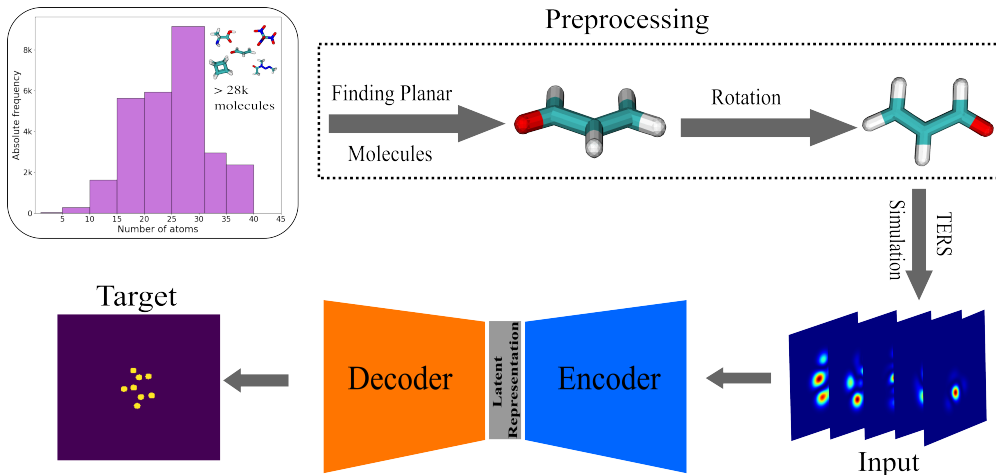


FIG. 2: Schematic of the deep learning workflow for structure prediction from TERS images.

of the simulation method first implemented by Zhang et al. [19]. The network is then trained in a supervised manner to learn a direct mapping from the TERS image to the atomic map, where pixel intensity represents the presence of an atom. The entire end-to-end pipeline is depicted in Fig. 2.

A. Molecule Dataset

For generating TERS simulated images, the geometries of sample molecules were taken from a well-known database of small organic molecules structurally optimized with density functional theory (DFT) [41]. The selected dataset was a sub-part of the original dataset chosen for establishing automating structure discovery in AFM – we initially selected a subset of 28,570 molecules containing up to 40 atoms as representative of commonly studied systems in TERS. From this subset, we systematically identified planar molecules by employing principal component analysis (PCA) to the atomic coordinates of each molecule. However, planarity alone was insufficient to ensure optimal TERS imaging conditions as planar molecules can be arbitrarily rotated, potentially obscuring parts of the structure from the tip’s view during a scan. We mitigated this by rotating each selected molecule to lie in the plane, perpendicular to the tip’s axis (see Appendix B for details). Following this preprocessing pipeline, the dataset was reduced to 1840 molecules, which were subsequently used to generate TERS hyperspectral images for model training. The statistical properties

of this set, including distributions of molecule size and elemental composition, are presented in 3.

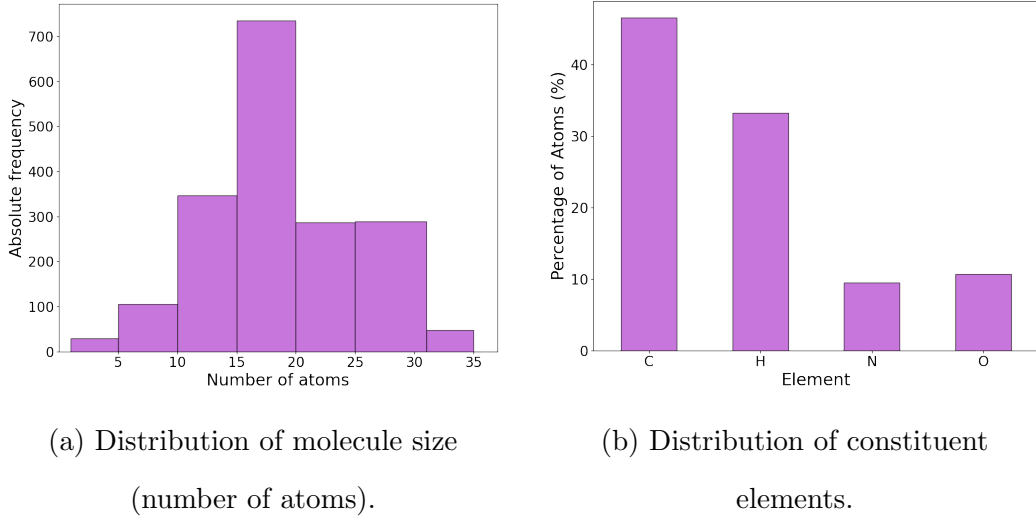


FIG. 3: Characteristics of the final dataset of 1,840 preprocessed planar molecules used for simulated TERS image generation.

B. Simulation Method

Our simulation approach to calculate the intensity of the Raman scattering is based on previous work [17, 18, 21–23, 39, 40], while the complete workflow of the simulation method is illustrated in Fig. 4. In SMARTERS, we ported the code developed by Yao Zhang *et al* [17] into python to ensure compatibility within our ML framework. The simulation technique decouples the calculation of contribution of the tip and the molecule. The contribution of the tip to the field environment is calculated using atomistic dipole-dipole attraction (DDA). Molecular polarizability derivatives can be computed directly from atomic contributions, which are then used to measure the Raman dipole moment. The total Raman dipole moment is subsequently employed to calculate the Raman scattering cross-section for each vibrational mode. By summing the contributions of all vibrational modes, the Raman point spectrum of the molecule is obtained. Finally, simulated TERS hyperspectral images corresponding to different vibrational modes are generated by combining spectral information from various spatial regions of the molecule. In our implementation, atomic polarizabilities were calculated using DFT with the Gaussian software package [42].

One of the most important parameters for the TERS simulated images is the size of the spatially confined plasmon. The more localized the plasmon, the more subtle features of the spatial distribution of the vibrational modes can be identified, thus enabling the model to better distinguish between structurally similar molecules. In contrast, a larger plasmon is not able to distinguish between important spectral features, reducing the prediction reliability of our model with respect to those features. Our images were then generated by setting a plasmonic size of 5 Å (represented by a 3D gaussian with FWHM of 5 Å), which was enough to distinguish, for example, features arising from Jahn–Teller distortions [23]. The simulation field of view was set to $18 \times 18 \text{ Å}^2$ so that the full lateral extent of the largest molecules is contained within the scan window. Smaller grids would truncate peripheral regions of the structure and effectively crop the simulated images. The hyperspectral maps were rasterised at 256×256 pixels to preserve spatial detail. Coarser discretisations reduced performance by limiting the model’s ability to distinguish vibrational mode signals from noise.

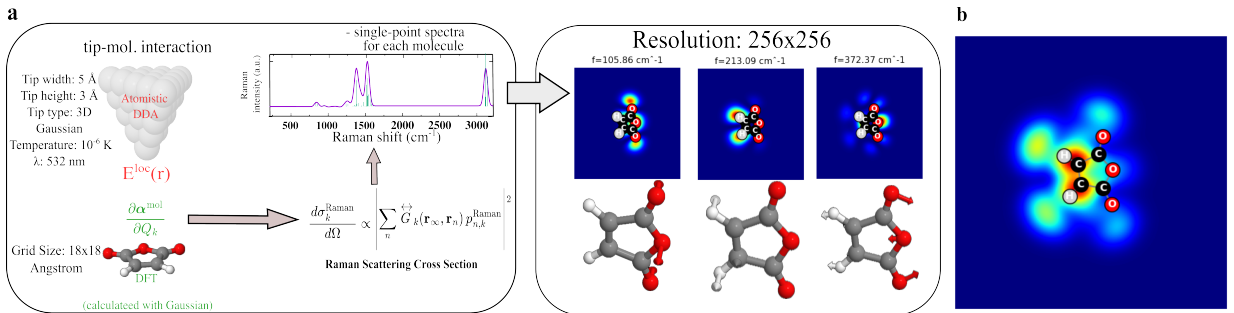


FIG. 4: **TERS Simulation Pipeline.** Our data generation process, adapted from Zhang et al. [17]. (a) The workflow takes a molecule’s geometry, calculates DFT properties, simulates interaction, and computes the Raman spectrum. (b) Sum of all TERS Hyperspectral images for visualization.

C. Image Dataset

Using the simulation method described above, we generated TERS hyperspectral image cubes for each of the 1,840 planar molecules in our dataset. A key challenge arose from the fact that different molecules exhibit varying numbers of vibrational modes, resulting in hyperspectral images with different numbers of spectral channels. To obtain

a uniform representation suitable for neural network training, we developed a binning procedure along the frequency axis. The binning strategy divides the frequency range of interest (0–4000 cm^{-1}) into n uniform bins, where the i -th bin covers the interval $\left[i \cdot \frac{4000}{n}, (i + 1) \cdot \frac{4000}{n} \right]$, $i = 0, 1, \dots, n - 1$. Each bin aggregates vibrational contributions within its frequency range, resulting in a standardized hyperspectral cube of size $H \times W \times n$, where H and W denote the spatial dimensions, and n represents the number of spectral bins (channels). This binning procedure provides two main advantages: 1) it produces hyperspectral cubes with a fixed number of channels across all molecules, enabling consistent model training; 2) it preserves coarse frequency localization of vibrational modes while reducing computational complexity.

We treated n as a hyperparameter and systematically compared different settings with $n = 400$ and $n = 100$. The region of interest for frequency was from 0–4000 cm^{-1} . Therefore, $n = 400$ corresponds to a spectral resolution of 10 cm^{-1} per bin, while $n = 100$ corresponds to 40 cm^{-1} per bin. Based on validation-set performance (Sec. III A), we determined that $n = 100$ provided better accuracy while simultaneously reducing training time due to the smaller input dimensionality.

D. Model training

The ML architecture of SMARTERS is similar to the encoder-decoder-type networks that have widely been used in computer vision problems, for example, image segmentation [43]. We selected the Attention U-Net architecture [44] as our structure discovery model, specifically configured to output a single-channel atomic map representing the predicted molecular structure. We chose this model motivated by its demonstrated prior success in automating structure discovery from scanning probe microscopy images [32, 34, 35]. The number of input channels of the model was treated as a hyperparameter to accommodate different spectral representations of the simulated TERS hyperspectral images as input, with either 100 or 400 channels depending on the binning strategy described in Section II C. This design allowed us to assess whether higher spectral resolution provides additional predictive benefit, or whether a reduced representation obtained by summing nearby frequency bands is sufficient.

The ML model operates through two main phases: feature extraction and structure

prediction. In the encoder phase, the network extracts spectroscopic features from each frequency channel as a function of their spectral character and spatial position. This process occurs simultaneously across all frequency channels in the hyperspectral data—spectroscopic features that appear consistently across multiple frequency channels and are more likely to be identified as structurally significant. As the network processes data through its multiple layers, it filters these spectroscopic features according to learned weights and biases, ultimately identifying critical feature maps that correlate with molecular structural elements. The decoder then reconstructs the 2D atomic map from these learned features, making predictions about atomic positions based on the spectroscopic input. The attention mechanism in the U-Net architecture is particularly valuable for TERS data analysis, as it allows the network to focus on the most informative spectral-spatial relationships while suppressing irrelevant background signals. This is crucial for TERS applications where signal-to-noise ratios can vary and specific vibrational modes may provide more structural information than others.

Our dataset of 1,840 planar molecules was split into 80/10/10 partitions for training, validation, and testing respectively. The network was trained for 50 epochs using the Adam optimizer [45]. Performance is quantified by the mean Dice Similarity Coefficient (DSC) [46], which measures the average of pixel-wise overlap between the predicted and ground-truth structures (see Section C 1 for more details). DSC loss is ideal for this structure prediction task as it directly optimizes for spatial overlap and is robust to the class imbalance between sparse atomic pixels and the background. Simple data augmentations were applied on-the-fly during training to encourage invariance to image orientation and robustness to additive noise, serving as a deliberately simplified proxy for common experimental variations. The augmentation pipeline included random rotations by multiples of 90° , horizontal and vertical flips, and additive Gaussian noise with standard deviation sampled uniformly from [0.01, 0.1]. Identical geometric transformations were applied to the input images and corresponding masks. Validation and test sets were kept unchanged.

To optimize model performance, we conducted a systematic exploration of key hyperparameters including batch size, learning rate, encoder/decoder depth, and the number of attention channels. We employed Bayesian optimization using the Optuna library [47] to efficiently navigate the hyperparameter space. The explored ranges and final selected values are summarized in Table I in Appendix A. Our entire implementation is built on the

PyTorch framework [48].

III. RESULTS

A. Performance evaluation of SMARTERS

We evaluate our proposed Attention U-Net model on the task of atomic position prediction for planar molecules. The model is trained to generate a labeled atom map from simulated images, where each atom is represented as a circle of fixed radius. Our model achieves a mean DSC of 0.862, 0.833 and 0.842 on the training, validation and test set respectively, demonstrating its efficacy in predicting the geometry of the molecule. The performance across the training, validation, and test splits remains consistent, indicating robust generalization.

To understand the factors influencing prediction accuracy, we investigated its relationship with molecular planarity. We hypothesized that performance would degrade for minor structural deviations, as the underlying TERS data acquisition is highly sensitive to nanoscopic changes in tip-molecule orientation. This sensitivity arises because deviations from ideal planarity alter the local electromagnetic field enhancement, causing a loss of key spectroscopic information. Our results, illustrated in Fig. 5, confirm this hypothesis. The plot of DSC against root mean square deviation (RMSD) shows a marked performance degradation for molecules with $\text{RMSD} > 0.01 \text{ \AA}$, characterized by a lower median DSC. This indicates that as molecules deviate from planarity, the model’s predictions become less accurate and less reliable. To examine this effect further, we trained models on datasets including more non-planar molecules, as will be shown in Sec. III B, confirming that higher RMSD correlates with lower DSC.

A qualitative analysis of the top and bottom 10% of test predictions, ordered by DSC, was performed to identify the factors influencing model performance. As shown in Figure 6, predictions in the top decile exhibit high fidelity, accurately reconstructing atomic arrangements where the TERS signal is strong and uniform. Conversely, the primary imperfect localization, illustrated in Figure 7, can be attributed to two main factors: (i) weak Raman signals from atoms located further from the tip, leading to reduced positional precision, and (ii) highly imbalanced Raman contribution of different bonds, which can bias the predicted

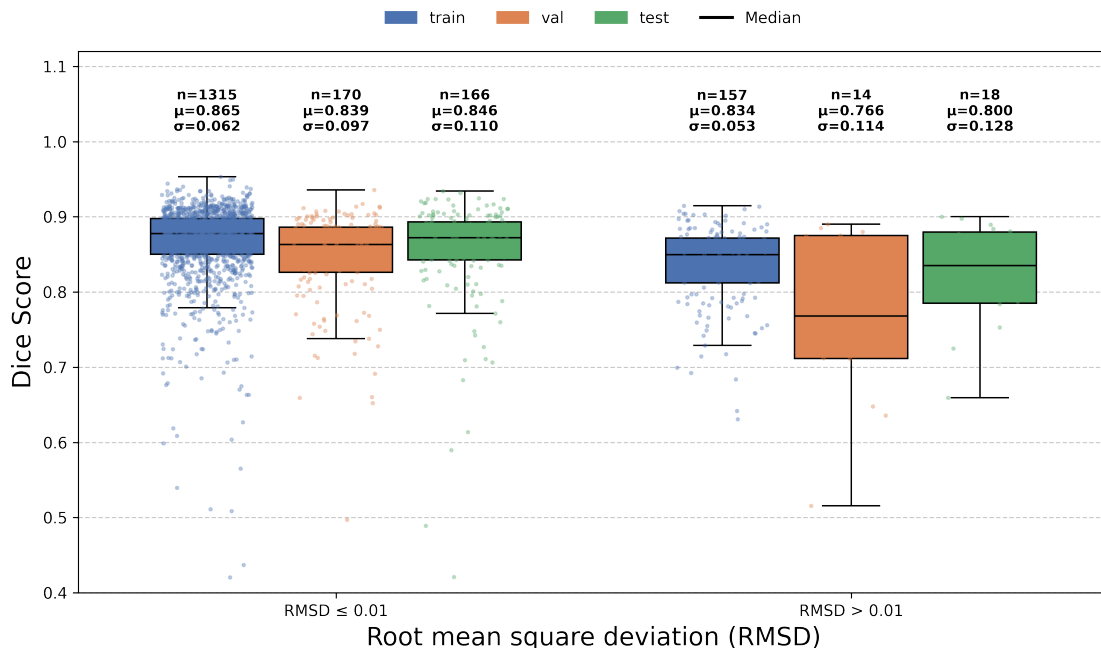


FIG. 5: Model performance as a function of planarity. Molecules that deviate more from being flat (RMSD $>$ 0.01 Å) show a noticeable drop in DSC, indicating that the model has more difficulty with non-planar structures.

geometry. Notably, even in these lower-ranked predictions, the model often generates chemically plausible structures, suggesting it has learned robust priors about molecular geometry even if the DSC is low. These limitations highlight clear directions for improving both future data acquisition protocols and model robustness.

B. Ablation study on the effect of planarity on the accuracy

Non-planar molecular geometries present an inherent challenge for TERS imaging because the near-field enhancement decays rapidly with increasing distance from the surface. Consequently, atomic contributions originating from out-of-plane atoms are attenuated and less consistently resolved, leading to increased variability in the measured signal for otherwise structurally similar molecules. We refer to this effect throughout as *planarity-induced variability* (PIV).

To investigate the influence of PIV on model performance, datasets were constructed using progressively relaxed planarity constraints. Four models were independently trained,

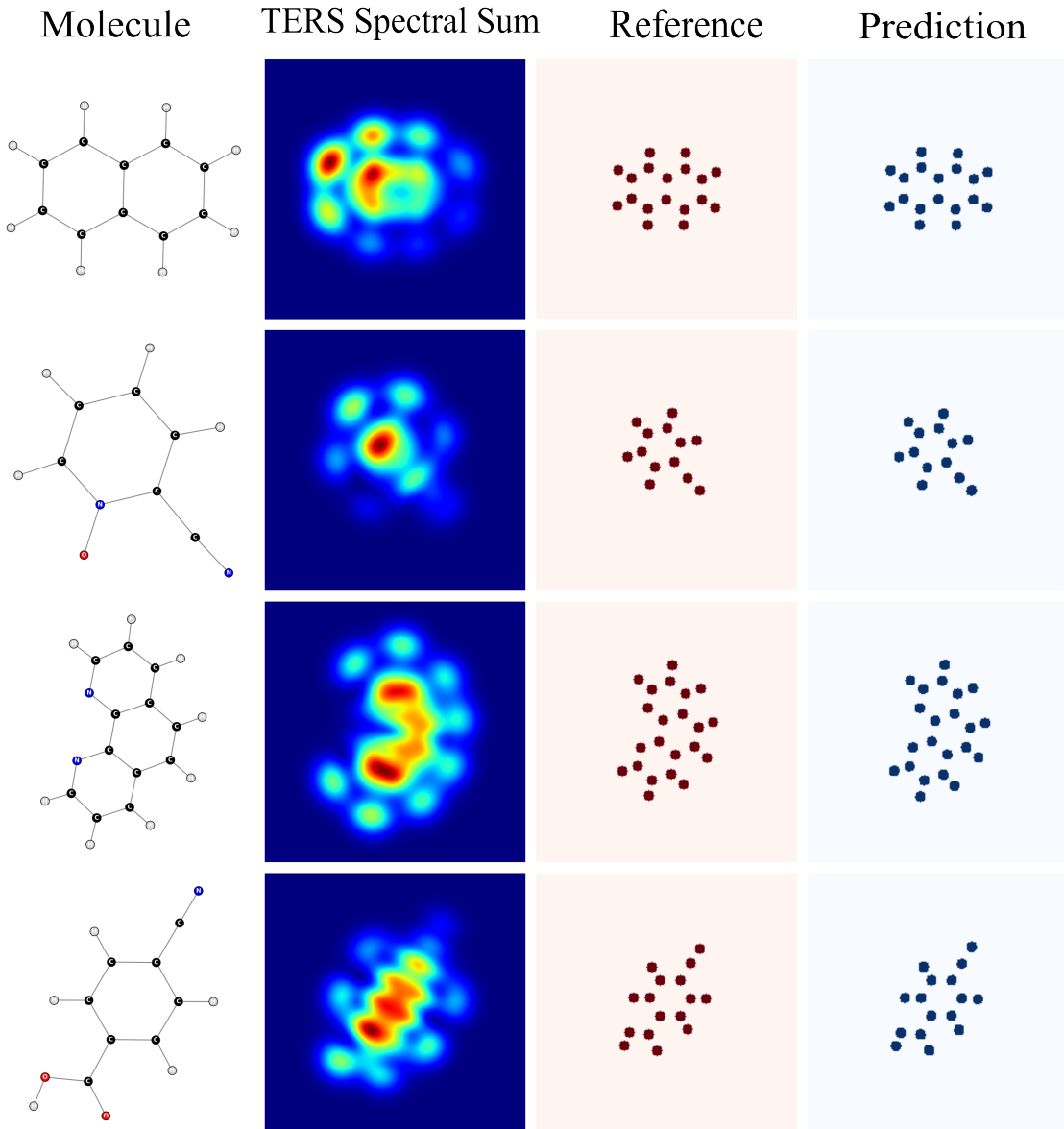


FIG. 6: **Representative examples of high-fidelity predictions (top 10% by DSC).** The model accurately reconstructs the atomic positions for molecules with strong, uniform TERS signals. Left: Ground Truth. Right: Model Prediction.

validated, and tested on datasets defined by RMSD thresholds of ≤ 0.05 , ≤ 0.1 and ≤ 0.5 Å, enabling a controlled investigation of increasing deviations from molecular planarity. As illustrated in Fig. 8, model performance degrades systematically as the fraction of non-planar molecules increases: median DSC decline while the spread of the performance distribution grows. This pattern is consistent across training, validation and test splits.

Although an increase in sample size would typically be expected to reduce variance un-

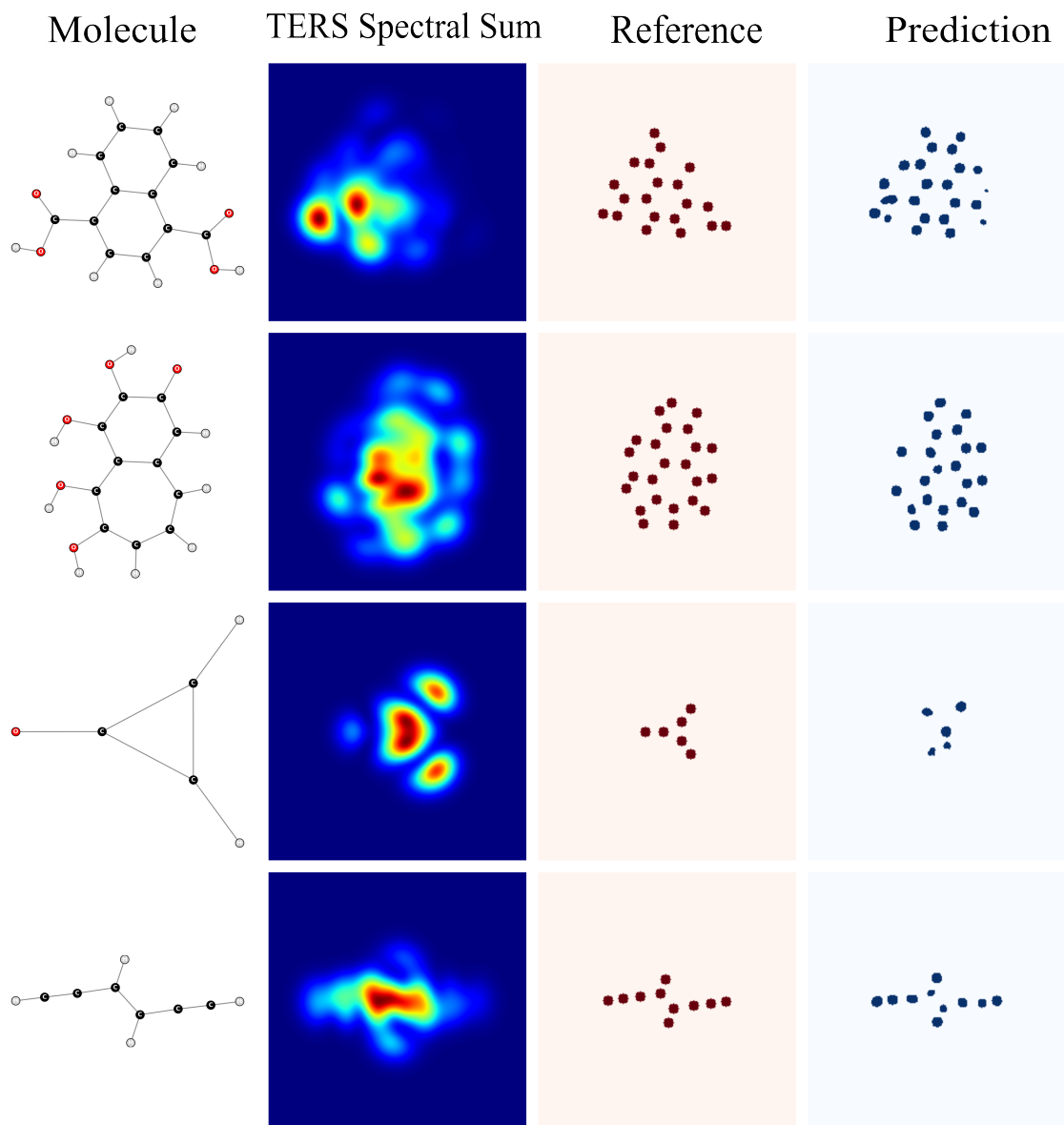
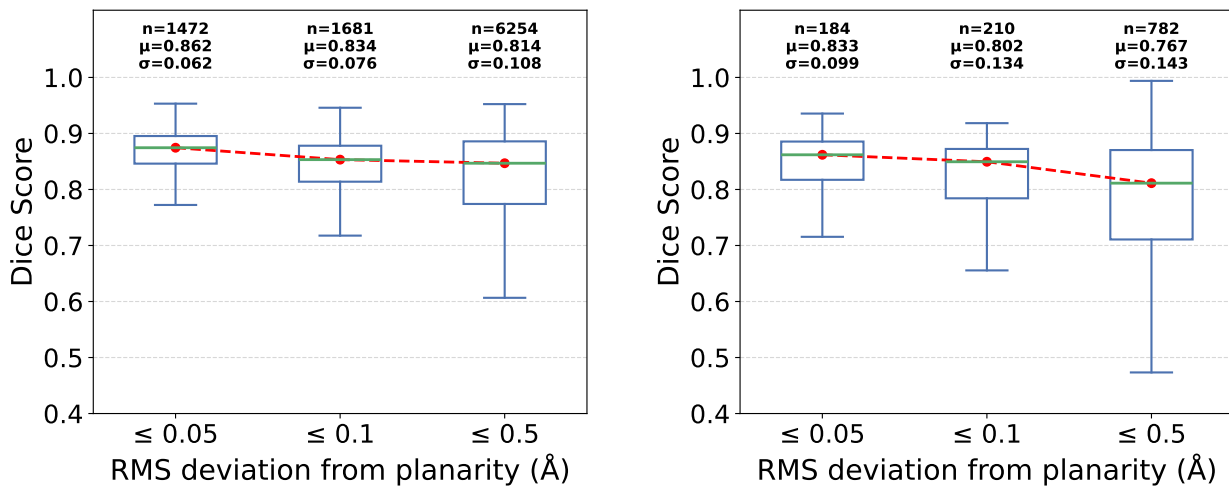


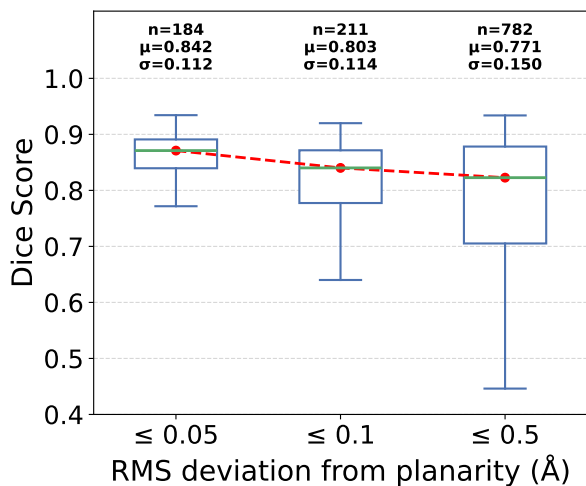
FIG. 7: **Characteristic imperfect localization of the model (bottom 10% by DSC).** Errors correlate with attenuated signals from distant atoms and geometric distortions from unequal bond signals.

der purely statistical assumptions, the observed increase in performance spread reflects the effect of PIV on the observed TERS signal intensity. Out-of-plane distortions alter the effective signal formation by weakening or obscuring near-field contributions. As a result, the mapping from molecular structure to measured signal becomes less deterministic. In other words, PIV increases the ambiguity of the inverse problem, which manifests as higher prediction variability for models trained on datasets containing greater structural planarity



(a) Training Set

(b) Validation Set



(c) Test Set

FIG. 8: **Impact of molecular planarity on DSC.** The x-axis represents a cumulative threshold ($\text{RMSD} < x$), where each bin includes all molecules with a planarity deviation less than the specified value in Å. The median trend line shows the decrease in the accuracy with increase in non-planarity. As the inclusion threshold increases (allowing less planar molecules), the variance in performance increases.

variation. This analysis highlights an important practical consideration for dataset curation in TERS-based machine learning. RMSD thresholds should be chosen to balance structural diversity against the physical limitations of near-field sensitivity: including molecules with pronounced out-of-plane distortion increases PIV and degrades model performance for the

present modelling approach.

Beyond PIV, TERS presents additional constraints arising from vibrational selection effects. Stretching modes are often weak or absent, and vibrational modes oriented predominantly parallel to the surface contribute less strongly to the measured signal, whereas modes normal to the surface or aligned with the tip axis dominate the response. This introduces ambiguity in defining the ground-truth image, since atomic groups exhibiting primarily in-plane vibrations may remain weakly represented or undetected in the measurements. Consequently, certain structural regions may appear absent in the signal despite being physically present, introducing inconsistencies that can further complicate model training.

IV. CONCLUSIONS

In this work, we introduced a deep learning framework termed SMARTERS capable of predicting molecular structures from simulated TERS hyperspectral images. By training an encoder-decoder network to map vibrational spectra to atomic coordinates, we demonstrate high fidelity in reconstructing planar molecular geometries from simulated images. This result establishes the viability of a ML-driven approach to bypass traditional, often ambiguous, manual interpretation, thereby opening a new avenue for automated molecular discovery from TERS.

While this study serves as a critical proof of concept, we identify three key areas for future research. First, extending the approach to non-planar systems remains an open challenge. The core difficulty is that atoms located beneath the surface do not contribute directly to the TERS signal but still influence the vibrational modes through their bonds. We posit that a transition from 2D representations to 3D molecular graphs, processed by graph neural networks, presents the most compelling path forward. Such a framework is not only essential for inferring the complete 3D geometry from the indirect vibrational contributions of subsurface atoms, but would also inherently provide robustness to molecular orientation and help disentangle the true signal from tip-positional artifacts. Second, beyond geometry, the rich chemical fingerprints within TERS spectra offer the potential for complete, chemically-resolved structure determination. Realizing this goal is contingent on overcoming the data limitations encountered in this study; the lack of chemical diversity in our planar molecule dataset made such an analysis impossible without introducing significant model bias. Fi-

nally, bridging the sim-to-real gap is paramount for practical application. Experience from ML models in SPM suggest that the model's ability to generalize to diverse experimental TERS data is contingent on training with larger datasets, enriched with complex augmentations that realistically simulate a wide variety of experimental conditions, including thermal noise, tip variations, and substrate effects.

V. ACKNOWLEDGEMENTS

The authors thank Krystof Brezina and Mariana Rossi for insightful discussions and helpful feedback. The work was supported by the Finnish Ministry of Education and Culture through the Quantum Doctoral Education Pilot Program (QDOC VN/3137/2024-OKM-4) and the Research Council of Finland through the Finnish Quantum Flagship project (358877, Aalto University). O.J.S. acknowledge the financial support from the Research Council of Finland No. 371875. The authors acknowledge the computational resources provided by the Aalto Science-IT Project and CSC.

Appendices

Appendix A: Model

The encoder-decoder structure used for structure discovery for TERS is Attention U-Net model originally introduced by Oktay *et al.* [44]. It uses U-Net architecture [49] with attention mechanism [50]. An overview of the network and the additive attention gate module is shown in Fig. 9. The model operates on 2-D TERS images and follows a symmetric encoder-decoder design (Fig. 9a). Each encoder stage consists of two successive 3×3 convolutional layers with batch normalisation and ReLU activation, followed by max pooling with a downsampling factor of 2.

In the encoder, the model learns hierarchical features by progressively reducing the spatial resolution while increasing the number of feature channels. The decoder mirrors this process using bilinear upsampling, concatenation with the corresponding encoder features, and convolutional refinement to recover spatial detail (Fig. 9a). The encoder-decoder depth and channel widths used in each configuration are reported in Table I. To suppress irrelevant encoder activations, skip connections are filtered using additive attention gates (Fig. 9b). Let $x_l \in \mathbb{R}^{C_l \times H_l \times W_l}$ denote the encoder feature map at level l , and let $g \in \mathbb{R}^{C_g \times H_l \times W_l}$ denote the decoder “gating” feature map from a coarser scale, resized to match the spatial resolution (H_l, W_l) . Both are linearly projected using 1×1 convolutions into a common intermediate space of C_{att} channels and combined to compute attention coefficients

$$\alpha_l = \sigma(\psi^\top \text{ReLU}(W_x x_l + W_g g + b)), \quad (\text{A1})$$

where W_x and W_g are learned 1×1 convolutional projections, b is a bias term, $\text{ReLU}(\cdot)$ is the rectified linear unit, and ψ^\top denotes a learned 1×1 projection mapping the intermediate representation to a single-channel attention logit. The sigmoid activation produces an attention map $\alpha_l \in [0, 1]^{1 \times H_l \times W_l}$. This map is applied channel-wise to the encoder features, yielding the gated representation $\tilde{x}_l = \alpha_l \odot x_l$, where \odot denotes element-wise multiplication. The gated features \tilde{x}_l are concatenated with decoder features before convolutional refinement. This mechanism allows decoder context to emphasise spatial regions consistent with the predicted molecular structure while suppressing background or noisy artefacts in simulated TERS images.

In contrast to the original medical-imaging implementation, our model processes 2-D

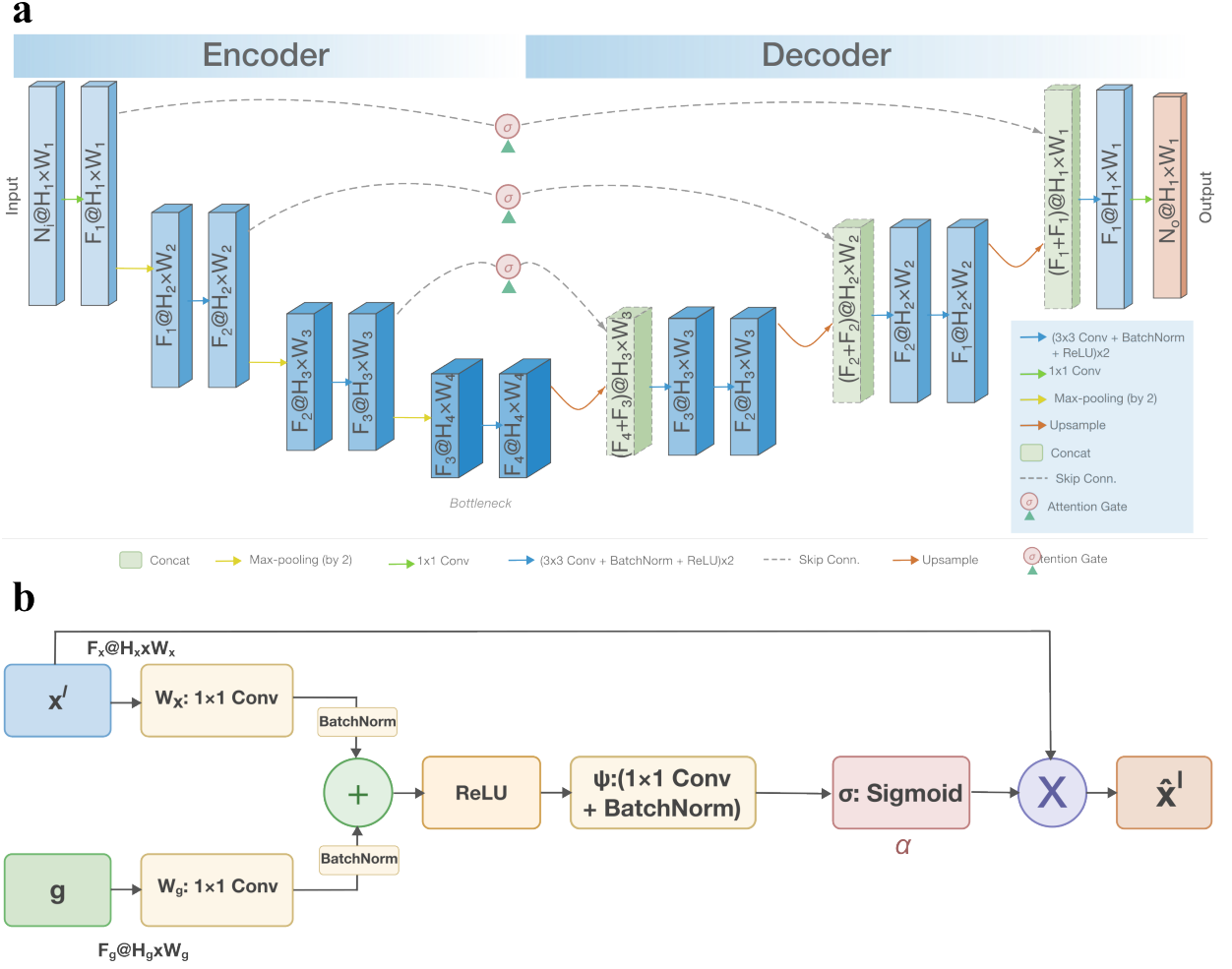


FIG. 9: (a) Attention U-Net architecture used for structure prediction from TERS images, illustrated here with a 3-level encoder/decoder depth, together with the additive attention gate applied on the skip connections. F_k denotes the number of filters at stage k , while N_i and N_o denote the input and output channels, respectively; $N_o = 1$ since the model predicts a single-channel binary structure mask (structure vs. background). (b) Additive attention gate for skip-connection filtering. Decoder context g is used to compute attention coefficients α_l that scale encoder features x_l , suppressing irrelevant activations prior to concatenation in the decoder..

inputs with configuration-dependent depth and channel widths. A final 1×1 convolution maps the last decoder features to the predicted structure mask. The resulting architecture retains U-Net's localisation capability, while attention gating conditions skip-feature transfer on decoder context, enabling selective integration of spatial detail relevant to the predicted structure.

TABLE I: Hyperparameter search space and selected model configurations for datasets constructed using different RMSD thresholds. For each threshold, we report the configuration achieving the best validation performance for the model trained on the corresponding dataset. Filter configurations define both the number of filters per stage and the encoder/decoder depth:

$$\begin{aligned} \mathbf{A} &= [16, 32, 64] \text{ (3-level)}, \mathbf{B} = [16, 32, 64, 128] \text{ (4-level)}, \\ \mathbf{C} &= [16, 32, 64, 128, 256] \text{ (5-level)}, \mathbf{D} = [32, 64, 128, 256, 512] \text{ (5-level)}. \end{aligned}$$

Hyperparameter	Search space	Selected value		
		0.05 Å	0.10 Å	0.50 Å
Input channels	{100, 400}	100	100	400
Encoder/decoder filters	{A, B, C, D}	C	B	D
Attention channels	{16, 32, 64}	16	16	32
Batch size	{16, 32, 64, 128}	16	32	16
Learning rate	$[10^{-5}, 10^{-3}]$	7.35×10^{-4}	5.56×10^{-4}	1.29×10^{-4}

Appendix B: Dataset Preprocessing

1. Principal Component Analysis for Planarity Selection and Tip Alignment

To ensure reliable TERS simulations in the current model, only planar molecules were included in the dataset. Planarity was determined using principal component analysis (PCA) on the 3D atomic coordinates $\mathbf{X} \in \mathbb{R}^{N \times 3}$, where N is the number of atoms. PCA decomposes the molecular coordinates into orthogonal axes of maximum variance by diagonalizing the covariance matrix:

$$\mathbf{C} = \frac{1}{N}(\mathbf{X} - \bar{\mathbf{X}})^\top(\mathbf{X} - \bar{\mathbf{X}}) \quad (\text{B1})$$

where $\bar{\mathbf{X}}$ is the mean atomic coordinate vector. The eigendecomposition of \mathbf{C} yields three eigenvalues $\lambda_1 \geq \lambda_2 \geq \lambda_3 \geq 0$ and a corresponding orthonormal set of eigenvectors $\{\mathbf{v}_1, \mathbf{v}_2, \mathbf{v}_3\}$. These eigenvalues quantify the variance of the atomic coordinates along the principal axes defined by the eigenvectors. The plane spanned by $\{\mathbf{v}_1, \mathbf{v}_2\}$ constitutes the

best-fit plane through the molecule, while \mathbf{v}_3 is the normal vector to this plane.

Planar molecules were identified by checking the variance along the axis perpendicular to the molecular plane. Specifically, a molecule was classified as planar if:

$$\lambda_3 < \epsilon \quad (\text{B2})$$

where λ_3 is the smallest eigenvalue corresponding to the axis with minimal variance, and ϵ is a small threshold indicating negligible out-of-plane deviation. This ensures that most atoms lie approximately within a single plane. Equivalently, $\sqrt{\lambda_3}$ corresponds to the root-mean-square out-of-plane deviation of the atoms from the best-fit plane, and the above criterion enforces negligible displacement normal to the plane.

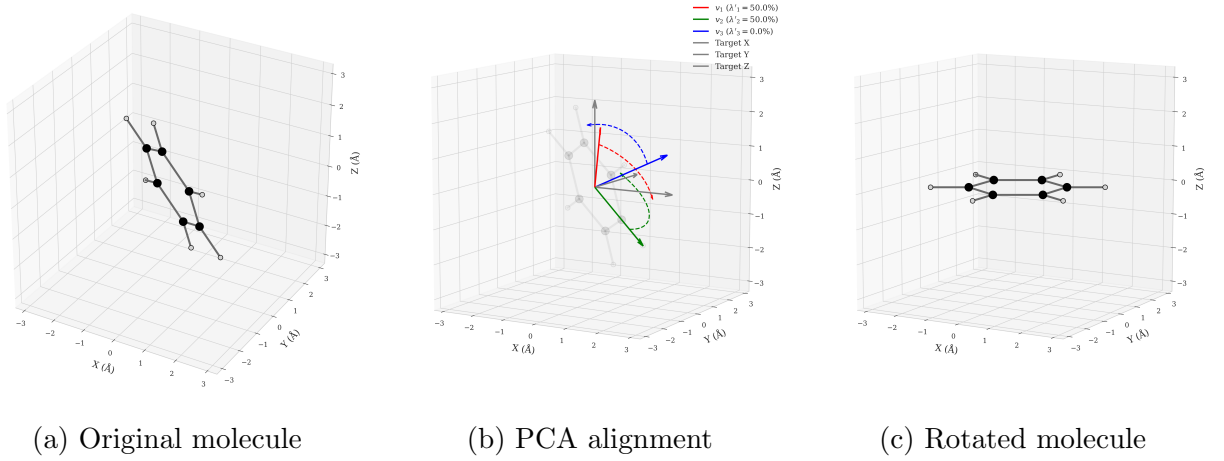


FIG. 10: Dataset preprocessing pipeline. (a) Original 3D coordinates of a molecule. (b) PCA identifies principal axes and eigenvalues; molecules with minimal out-of-plane variance ($\lambda_3 < \epsilon$) are selected as planar. (c) Selected planar molecules are rotated using rotation matrix \mathbf{R} so the molecular plane lies in the XY-plane and the tip is along the Z-axis, ensuring consistent orientation for TERS simulations.

After planar molecules were selected, each molecule was rotated to align its plane perpendicular to the TERS tip. Let \mathbf{R} be the rotation matrix constructed from PCA eigenvectors. The coordinates were transformed as:

$$\mathbf{X}_{\text{aligned}} = \mathbf{R}(\mathbf{X} - \bar{\mathbf{X}}) \quad (\text{B3})$$

The rotation aligns the molecular plane with the XY-plane and the tip along the Z-axis,

providing consistent orientation across all molecules and maximal structural visibility in TERS simulations.

Appendix C: Evaluation metrics

1. Dice Similarity Coefficient

The Dice similarity coefficient (DSC) is closely related to Intersection over Union (IoU) but gives more weight to the overlap between prediction and ground truth. It is defined as:

$$\text{Dice}(P, G) = \frac{2|P \cap G|}{|P| + |G|} \quad (\text{C1})$$

Like IoU, its value lies between 0 and 1, with higher scores indicating greater similarity. Both IoU and DSC provide complementary perspectives on segmentation accuracy, but the DSC emphasizes overlap accurately and is less sensitive to class imbalance.

-
- [1] Fabian Mohn, Jascha Repp, Leo Gross, Gerhard Meyer, Matthew S. Dyer, and Mats Persson. Reversible bond formation in a gold-atom-organic-molecule complex as a molecular switch. *Phys. Rev. Lett.*, 105:266102, Dec 2010. doi: 10.1103/PhysRevLett.105.266102. URL <https://link.aps.org/doi/10.1103/PhysRevLett.105.266102>.
- [2] Prokop Hapala, Georgy Kichin, Christian Wagner, F. Stefan Tautz, Ruslan Temirov, and Pavel Jelínek. Mechanism of high-resolution stm/afm imaging with functionalized tips. *Phys. Rev. B*, 90:085421, Aug 2014. doi: 10.1103/PhysRevB.90.085421. URL <https://link.aps.org/doi/10.1103/PhysRevB.90.085421>.
- [3] Kewei Sun, Orlando J. Silveira, Yujing Ma, Yuri Hasegawa, Michio Matsumoto, Satoshi Kera, Ondřej Krejčí, Adam S. Foster, and Shigeki Kawai. On-surface synthesis of disilabenzene-bridged covalent organic frameworks. *Nature Chemistry*, 15(1):136–142, Jan 2023. ISSN 1755-4349. doi: 10.1038/s41557-022-01071-3. URL <https://doi.org/10.1038/s41557-022-01071-3>.
- [4] Niko Oinonen, Aliaksandr V. Yakutovich, Aurelio Gallardo, Martin Ondráček, Prokop Hapala, and Ondřej Krejčí. Advancing scanning probe microscopy simulations: A decade

- of development in probe-particle models. *Computer Physics Communications*, 305:109341, 2024. ISSN 0010-4655. doi: <https://doi.org/10.1016/j.cpc.2024.109341>. URL <https://www.sciencedirect.com/science/article/pii/S0010465524002649>.
- [5] Leo Gross, Fabian Mohn, Nikolaj Moll, Peter Liljeroth, and Gerhard Meyer. The chemical structure of a molecule resolved by atomic force microscopy. page 1110. doi: 10.1126/science.1176210. URL <https://www.science.org/doi/abs/10.1126/science.1176210>. tex.ids=gross_chemical_2009, gross_chemical_2009-1 publisher: American Association for the Advancement of Science.
- [6] Leo Gross, Fabian Mohn, Nikolaj Moll, Bruno Schuler, Alejandro Criado, Enrique Guitián, Diego Peña, André Gourdon, and Gerhard Meyer. Bond-order discrimination by atomic force microscopy. *Science*, 337(6100):1326–1329, 2012. doi: 10.1126/science.1225621. URL <https://www.science.org/doi/abs/10.1126/science.1225621>.
- [7] Fabian Schulz, Juha Ritala, Ondrej Krejčí, Ari Paavo Seitsonen, Adam S. Foster, and Peter Liljeroth. Elemental identification by combining atomic force microscopy and kelvin probe force microscopy. *ACS Nano*, 12(6):5274–5283, 2018. doi: 10.1021/acsnano.7b08997. URL <https://doi.org/10.1021/acsnano.7b08997>. PMID: 29800512.
- [8] E. Abbe Hon. Vii.—on the estimation of aperture in the microscope. *Journal of the Royal Microscopical Society*, 1(3):388–423, 1881. doi: <https://doi.org/10.1111/j.1365-2818.1881.tb05909.x>. URL <https://onlinelibrary.wiley.com/doi/abs/10.1111/j.1365-2818.1881.tb05909.x>.
- [9] Tamitake Itoh, Marek Procházka, Zhen-Chao Dong, Wei Ji, Yuko S. Yamamoto, Yao Zhang, and Yukihiro Ozaki. Toward a new era of sers and ters at the nanometer scale: From fundamentals to innovative applications. *Chemical Reviews*, 123(4):1552–1634, 2023. doi: 10.1021/acs.chemrev.2c00316. URL <https://doi.org/10.1021/acs.chemrev.2c00316>. PMID: 36745738.
- [10] Alyssa B. Zrimsek, Naihao Chiang, Michael Mattei, Stephanie Zaleski, Michael O. McAnally, Craig T. Chapman, Anne-Isabelle Henry, George C. Schatz, and Richard P. Van Duyne. Single-molecule chemistry with surface- and tip-enhanced raman spectroscopy. *Chemical Reviews*, 117(11):7583–7613, 2017. doi: 10.1021/acs.chemrev.6b00552. URL <https://doi.org/10.1021/acs.chemrev.6b00552>. PMID: 28610424.
- [11] Ben Yang, Gong Chen, Atif Ghaffoor, Yu-Fan Zhang, Xian-Biao Zhang, Hang Li, Xiao-Ru

- Dong, Rui-Pu Wang, Yang Zhang, Yao Zhang, and Zhen-Chao Dong. Chemical enhancement and quenching in single-molecule tip-enhanced raman spectroscopy. *Angewandte Chemie International Edition*, 62(13):e202218799, 2023. doi: <https://doi.org/10.1002/anie.202218799>. URL <https://onlinelibrary.wiley.com/doi/abs/10.1002/anie.202218799>.
- [12] Joonhee Lee, Kevin T. Crampton, Nicholas Tallarida, and V. Ara Apkarian. Visualizing vibrational normal modes of a single molecule with atomically confined light. *Nature*, 568(7750):78–82, Apr 2019. ISSN 1476-4687. doi: 10.1038/s41586-019-1059-9. URL <https://doi.org/10.1038/s41586-019-1059-9>.
- [13] Song Jiang, Xianbiao Zhang, Yao Zhang, Chunrui Hu, Rui Zhang, Yang Zhang, Yuan Liao, Zachary J. Smith, Zhenchao Dong, and J. G. Hou. Subnanometer-resolved chemical imaging via multivariate analysis of tip-enhanced raman maps. *Light: Science & Applications*, 6(11):e17098–e17098, Nov 2017. ISSN 2047-7538. doi: 10.1038/lsa.2017.98. URL <https://doi.org/10.1038/lsa.2017.98>.
- [14] Takashi Kumagai, Kuniyuki Miwa, and Borja Cirera. Point-contact tip-enhanced raman spectroscopy: Picoscale light–matter interactions within plasmonic cavities. *Nano Letters*, 25(43):15449–15459, 2025. doi: 10.1021/acs.nanolett.5c04045. URL <https://doi.org/10.1021/acs.nanolett.5c04045>. PMID: 41086349.
- [15] Rodrigo Cezar de Campos Ferreira, Borja Cirera, Jiří Doležal, Álvaro Gallego de Roa, Amandeep Sagwal, Petr Kahan, Rubén Canales, Fernando Aguilar-Galindo, Martin Švec, and Pablo Merino. Adsorption-driven symmetry lowering in single molecules revealed by ångstrom-scale tip-enhanced raman imaging, 2026. URL <https://arxiv.org/abs/2601.14110>.
- [16] Christiane Höppener, Javier Aizpurua, Huan Chen, Stefanie Gräfe, Ado Jorio, Stephan Kupfer, Zhenglong Zhang, and Volker Deckert. Tip-enhanced raman scattering. *Nature Reviews Methods Primers*, 4(1):47, Jul 2024. ISSN 2662-8449. doi: 10.1038/s43586-024-00323-5. URL <https://doi.org/10.1038/s43586-024-00323-5>.
- [17] Yao Zhang, Zhen-Chao Dong, and Javier Aizpurua. Theoretical treatment of single-molecule scanning raman picoscopy in strongly inhomogeneous near fields. *Journal of Raman Spectroscopy*, 52(2):296–309, 2021. doi: <https://doi.org/10.1002/jrs.5991>. URL <https://analyticalsciencejournals.onlinelibrary.wiley.com/doi/abs/10.1002/jrs.5991>.
- [18] Sai Duan, Guangjun Tian, Yongfei Ji, Jiushu Shao, Zhenchao Dong, and Yi Luo. Theoretical modeling of plasmon-enhanced raman images of a single molecule with subnanometer

- resolution. *Journal of the American Chemical Society*, 137(30):9515–9518, Aug 2015. ISSN 0002-7863. doi: 10.1021/jacs.5b03741. URL <https://doi.org/10.1021/jacs.5b03741>.
- [19] Yao Zhang, Ruben Esteban, Jie Cui, and Javier Aizpurua. Software to implement simulations of raman spectra of single-molecules in an inhomogeneous field, 2023.
- [20] Yair Litman, Franco P. Bonafé, Alaa Akkoush, Heiko Appel, and Mariana Rossi. First-principles simulations of tip enhanced raman scattering reveal active role of substrate on high-resolution images. *The Journal of Physical Chemistry Letters*, 14(30):6850–6859, 2023. doi: 10.1021/acs.jpcllett.3c01216. URL <https://doi.org/10.1021/acs.jpcllett.3c01216>. PMID: 37487223.
- [21] Xing Chen, Pengchong Liu, Zhongwei Hu, and Lasse Jensen. High-resolution tip-enhanced raman scattering probes sub-molecular density changes. *Nature Communications*, 10(1):2567, Jun 2019. ISSN 2041-1723. doi: 10.1038/s41467-019-10618-x. URL <https://doi.org/10.1038/s41467-019-10618-x>.
- [22] Feifei Qiu, Zu-Yong Gong, Dongwei Cao, Ce Song, Guangjun Tian, Sai Duan, and Yi Luo. Optical images of molecular vibronic couplings from tip-enhanced fluorescence excitation spectroscopy. *JACS Au*, 2(1):150–158, Jan 2022. doi: 10.1021/jacsau.1c00442. URL <https://doi.org/10.1021/jacsau.1c00442>.
- [23] Hai-Zhen Yu, Rui-Lin Han, Dingwei Chu, Yuanzhi Li, Xiao-Ru Dong, Yang Zhang, Li Wang, Yuzhi Song, Chuan-Kui Wang, Zhen Xie, and Sai Duan. Theoretical prediction for monitoring jahn-teller vibrational evolution using real-space tip-enhanced raman imaging. *Nature Communications*, 17(1):1132, Jan 2026. ISSN 2041-1723. doi: 10.1038/s41467-025-67894-z. URL <https://doi.org/10.1038/s41467-025-67894-z>.
- [24] Krystof Brezina, Yair Litman, and Mariana Rossi. Tip-enhanced raman images of realistic systems through ab initio modeling. *ACS Nano*, Feb 2026. ISSN 1936-0851. doi: 10.1021/acsnano.5c16052. URL <https://doi.org/10.1021/acsnano.5c16052>.
- [25] Xinzhong Chen, Suheng Xu, Sara Shabani, Yueqi Zhao, Matthew Fu, Andrew J. Millis, Michael M. Fogler, Abhay N. Pasupathy, Mengkun Liu, and D. N. Basov. Machine learning for optical scanning probe nanoscopy. *Advanced Materials*, 35(34):2109171, 2023. doi: <https://doi.org/10.1002/adma.202109171>. URL <https://advanced.onlinelibrary.wiley.com/doi/abs/10.1002/adma.202109171>.
- [26] Naresh Kumar, Li-Qing Zheng, Andrew J. Pollard, Andrew J. Wain, and Renato Zenobi.

- Nanoscale chemical analysis of heterogeneous catalysts using tip-enhanced raman spectroscopy. *Chemical Reviews*, Feb 2026. ISSN 0009-2665. doi: 10.1021/acs.chemrev.5c00707. URL <https://doi.org/10.1021/acs.chemrev.5c00707>.
- [27] Maxim Ziatdinov, Artem Maksov, and Sergei V. Kalinin. Learning surface molecular structures via machine vision. *npj Computational Materials*, 3(1), 8 2017. doi: 10.1038/s41524-017-0038-7.
- [28] Abid Khan, Chia-Hao Lee, Pinshane Y. Huang, and Bryan K. Clark. Leveraging generative adversarial networks to create realistic scanning transmission electron microscopy images. *npj Computational Materials*, 9(1):85, 2023. doi: 10.1038/s41524-023-01042-3. URL <https://doi.org/10.1038/s41524-023-01042-3>.
- [29] Kamal Choudhary. Microscopygpt: Generating atomic-structure captions from microscopy images of 2d materials with vision-language transformers. *The Journal of Physical Chemistry Letters*, 16(27):7028–7035, 2025. doi: 10.1021/acs.jpcllett.5c01257. URL <https://doi.org/10.1021/acs.jpcllett.5c01257>. PMID: 40590052.
- [30] Sergei V. Kalinin, Evgheni Strelcov, Alex Belianinov, Suhas Somnath, Rama K. Vasudevan, Eric J. Lingerfelt, Richard K. Archibald, Chaomei Chen, Roger Proksch, Nouamane Laanait, and Stephen Jesse. Big, deep, and smart data in scanning probe microscopy. 10(10):9068–9086. doi: 10.1021/acsnano.6b04212.
- [31] Md Ashiqur Rahman Laskar and Umberto Celano. Scanning probe microscopy in the age of machine learning. 1(4):041501. ISSN 2770-9019. doi: 10.1063/5.0160568. URL <https://pubs.aip.org/aml/article/1/4/041501/2920721/Scanning-probe-microscopy-in-the-age-of-machine>.
- [32] Benjamin Alldritt, Prokop Hapala, Niko Oinonen, Fedor Urtev, Ondrej Krejci, Filippo Federici Canova, Juho Kannala, Fabian Schulz, Peter Liljeroth, and Adam S. Foster. Automated structure discovery in atomic force microscopy. *Science Advances*, 6(9):eaay6913, 2020. doi: 10.1126/sciadv.aay6913. URL <https://www.science.org/doi/abs/10.1126/sciadv.aay6913>.
- [33] Binze Tang, Yizhi Song, Mian Qin, Ye Tian, Zhen Wei Wu, Ying Jiang, Duanyun Cao, and Limei Xu. Machine learning-aided atomic structure identification of interfacial ionic hydrates from AFM images. 10(7):nwac282. ISSN 2095-5138. doi: 10.1093/nsr/nwac282. URL <https://doi.org/10.1093/nsr/nwac282>.
- [34] N. Oinonen, L. Kurki, A. Ilin, and A. S. Foster. Molecule graph reconstruction from atomic

- force microscope images with machine learning. *MRS Bulletin*, 47(9):895–905, 2022. doi: 10.1557/s43577-022-00324-3.
- [35] Lauri Kurki, Niko Oinonen, and Adam S. Foster. Automated structure discovery for scanning tunneling microscopy. *ACS Nano*, 18(17):11130–11138, Apr 2024. ISSN 1936-0851. doi: 10.1021/acsnano.3c12654. URL <https://doi.org/10.1021/acsnano.3c12654>.
- [36] Fabio Priante, Niko Oinonen, Ye Tian, Dong Guan, Chen Xu, Shuning Cai, Peter Liljeroth, Ying Jiang, and Adam S. Foster. Structure discovery in atomic force microscopy imaging of ice. *ACS Nano*, 18(7):5546–5555, 2024. doi: 10.1021/acsnano.3c10958. URL <https://doi.org/10.1021/acsnano.3c10958>. PMID: 38315583.
- [37] Jaime Carracedo-Cosme, Carlos Romero-Muñiz, Pablo Pou, and Rubén Pérez. Molecular identification from afm images using the iupac nomenclature and attribute multimodal recurrent neural networks. *ACS Applied Materials & Interfaces*, 15(18):22692–22704, 2023. doi: 10.1021/acsami.3c01550. URL <https://doi.org/10.1021/acsami.3c01550>. PMID: 37126486.
- [38] Jaime Carracedo-Cosme and Rubén Pérez. Molecular identification with atomic force microscopy and conditional generative adversarial networks. *npj Computational Materials*, 10(1):19, 2024. doi: 10.1038/s41524-023-01179-1. URL <https://doi.org/10.1038/s41524-023-01179-1>.
- [39] Sai Duan, Guangjun Tian, and Yi Luo. Visualization of vibrational modes in real space by tip-enhanced non-resonant raman spectroscopy. *Angewandte Chemie International Edition*, 55(3):1041–1045, 2016. doi: <https://doi.org/10.1002/anie.201508218>. URL <https://onlinelibrary.wiley.com/doi/abs/10.1002/anie.201508218>.
- [40] Yuanzhi Li, Dingwei Chu, Wentao Ma, Hai-Zhen Yu, Yuzhi Song, Chuan-Kui Wang, Sai Duan, and Zhen Xie. Visualization of hydrogen isotope exchange in single molecule by tip-enhanced raman images. *The Journal of Chemical Physics*, 163(22):224310, 12 2025. ISSN 0021-9606. doi: 10.1063/5.0293414. URL <https://doi.org/10.1063/5.0293414>.
- [41] Niko Oinonen, Chen Xu, Benjamin Alldritt, Filippo Federici Canova, Fedor Urtev, Shuning Cai, Ondřej Krejčí, Juho Kannala, Peter Liljeroth, and Adam S. Foster. Electrostatic discovery atomic force microscopy. *ACS Nano*, 16(1):89–97, 2022. doi: 10.1021/acsnano.1c06840. URL <https://doi.org/10.1021/acsnano.1c06840>. PMID: 34806866.
- [42] M. J. Frisch, G. W. Trucks, H. B. Schlegel, G. E. Scuseria, M. A. Robb, J. R. Cheeseman,

- G. Scalmani, V. Barone, G. A. Petersson, H. Nakatsuji, X. Li, M. Caricato, A. V. Marenich, J. Bloino, B. G. Janesko, R. Gomperts, B. Mennucci, H. P. Hratchian, J. V. Ortiz, A. F. Izmaylov, J. L. Sonnenberg, D. Williams-Young, F. Ding, F. Lipparini, F. Egidi, J. Goings, B. Peng, A. Petrone, T. Henderson, D. Ranasinghe, V. G. Zakrzewski, J. Gao, N. Rega, G. Zheng, W. Liang, M. Hada, M. Ehara, K. Toyota, R. Fukuda, J. Hasegawa, M. Ishida, T. Nakajima, Y. Honda, O. Kitao, H. Nakai, T. Vreven, K. Throssell, J. A. Montgomery, Jr., J. E. Peralta, F. Ogliaro, M. J. Bearpark, J. J. Heyd, E. N. Brothers, K. N. Kudin, V. N. Staroverov, T. A. Keith, R. Kobayashi, J. Normand, K. Raghavachari, A. P. Rendell, J. C. Burant, S. S. Iyengar, J. Tomasi, M. Cossi, J. M. Millam, M. Klene, C. Adamo, R. Cammi, J. W. Ochterski, R. L. Martin, K. Morokuma, O. Farkas, J. B. Foresman, and D. J. Fox. Gaussian~16 Revision C.01, 2016. Gaussian Inc. Wallingford CT.
- [43] Vijay Badrinarayanan, Alex Kendall, and Roberto Cipolla. Segnet: A deep convolutional encoder-decoder architecture for image segmentation. *IEEE Transactions on Pattern Analysis and Machine Intelligence*, 39(12):2481–2495, 2017. doi: 10.1109/TPAMI.2016.2644615.
- [44] Ozan Oktay, Jo Schlemper, Loic Le Folgoc, Matthew Lee, Mattias Heinrich, Kazunari Misawa, Kensaku Mori, Steven McDonagh, Nils Y Hammerla, Bernhard Kainz, Ben Glocker, and Daniel Rueckert. Attention u-net: Learning where to look for the pancreas. In *Medical Imaging with Deep Learning*, 2018. URL <https://openreview.net/forum?id=Skft7cijM>.
- [45] Diederik P. Kingma and Jimmy Ba. Adam: A method for stochastic optimization, 2017. URL <https://arxiv.org/abs/1412.6980>.
- [46] Lee R. Dice. Measures of the amount of ecologic association between species. 26(3):297–302. ISSN 0012-9658. doi: 10.2307/1932409. URL <https://www.jstor.org/stable/1932409>.
- [47] Takuya Akiba, Shotaro Sano, Toshihiko Yanase, Takeru Ohta, and Masanori Koyama. Optuna: A next-generation hyperparameter optimization framework. In *Proceedings of the 25th ACM SIGKDD International Conference on Knowledge Discovery and Data Mining*, 2019.
- [48] Adam Paszke, Sam Gross, Francisco Massa, Adam Lerer, James Bradbury, Gregory Chanan, Trevor Killeen, Zeming Lin, Natalia Gimelshein, Luca Antiga, Alban Desmaison, Andreas Kopf, Edward Yang, Zachary DeVito, Martin Raison, Alykhan Tejani, Sasank Chilamkurthy, Benoit Steiner, Lu Fang, Junjie Bai, and Soumith Chintala. Pytorch: An imperative style, high-performance deep learning library. *Advances in Neural Information Processing Systems*, 32:8024–8035, 2019.

- [49] Olaf Ronneberger, Philipp Fischer, and Thomas Brox. U-net: Convolutional networks for biomedical image segmentation. In *Medical Image Computing and Computer-Assisted Intervention (MICCAI)*, pages 234–241. Springer, 2015. doi: 10.1007/978-3-319-24574-4_28.
- [50] Ashish Vaswani, Noam Shazeer, Niki Parmar, Jakob Uszkoreit, Llion Jones, Aidan N. Gomez, Lukasz Kaiser, and Illia Polosukhin. Attention is all you need, 2023. URL <https://arxiv.org/abs/1706.03762>.